Bandwidth-unlimited polarization-maintaining metasurfaces

Q. Song, S. Khadir, S. Vézian, B. Damilano, P. D. Mierry, S. Chenot, V. Brandli, P. Genevet*

Any arbitrary state of polarization of light beam can be decomposed into a linear superposition of two orthogonal oscillations, each of which has a specific amplitude of the electric field. The dispersive nature of diffractive and refractive optical components generally affects these amplitude responses over a small wavelength range, tumbling the light polarization properties. Although recent works suggest the realization of broadband nanophotonic interfaces that can mitigate frequency dispersion, their usage for arbitrary polarization control remains elusively chromatic. Here, we present a general method to address broadband full-polarization properties of diffracted fields using an original superposition of circular polarization beams transmitted through metasurfaces. The polarization-maintaining metasurfaces are applied for complex broadband wavefront shaping, including beam deflectors and white-light holograms. Eliminating chromatic dispersion and dispersive polarization response of conventional diffractive elements lead to broadband polarization-maintaining devices of interest for applications in polarization imaging, broadband-polarimetry, augmented/virtual reality imaging, full color display, etc.

INTRODUCTION

Polarization, one of the key parameters of electromagnetic wave, plays an important role in many areas, such as three-dimensional stereoscopic displays, quantum computation, chemical sensing, etc. Conventional generation method of arbitrary polarization involves bulky optical components combining polarizers and waveplates. In recent years, metasurfaces with optically thin thickness have been proposed by locally designing subwavelength structures to control all of the parameters of the electromagnetic wave, such as phase [1, 2], frequency [3], amplitude [4], propagation direction [5, 6], and polarization [7–10], leading to various applications, including lenses [11], cloaking [12], sensing [13, 14], information security [15], etc. The manipulation of polarization state of light using metasurfaces usually relies on designing the structural properties of anisotropic [16] and chiral nanostructures [17]. The superposition of two orthogonal polarizations has been proposed to generate versatile output polarization, simply by controlling the offset between the two polarization components [18, 19]. However, to generate full arbitrary polarization, the amplitude difference of the two polarization components has to be precisely controlled [20]. Amplitude control has generally been performed through the nanostructure geometric sizes, at the expense of introducing a huge dispersion of the amplitude response, compromising the device broadband operation, as schematically shown in Fig. 1 (A and B) .

Here, we propose a general method to maintain the full-polarization state of diffracted signal, essentially over an unlimited wavelength range, using appropriate superposition of orthogonal circular polarization (CP) (see schematic in Fig. 1, C and D). We also prove that our approach is compatible with basic chromatic dispersion compensation using a simple metasurface doublet (see schematic in Fig. 1, E and F), thus demonstrating a broadband white-light holographic image with broadband polarization-maintaining performances. The control of polarization helicity, i.e., left CP (LCP) or right CP (RCP), and the direction of the scattered light are controlled through an arrangement of spatially oriented birefringent geometric phase metastructures. This peculiar method to address wavefront ranging from basic beam deflection to complex holographic field distribution [21–28] relies on replication and rotation of a unique nanostructure. In general, the intrinsic dispersive modal response of the nanostructure creates strong dispersive response, but in this contribution, we report an interesting superposition regime for which the dispersive contribution of the antenna does not comprehend the overall polarization response. The method consists in superposing: (i) diffracted fields with the same handiness of CP to control the output light amplitude, essentially relying on simple interference condition, and (ii) an additional phase-retarded diffracted field oscillating on the opposite handiness, to access full polarization of the output light. Previously, vectorial meta-hologram able to address the problem of polarization-dependent image projection has been proposed, increasing the design degrees of freedom to enable polarization multiplexing [29–34]. A reflective meta-hologram based on diatomic metasurface has been proposed for the full polarized meta-hologram at oblique incidence [35, 36]. Full polarized meta-hologram can also be realized by combining geometric phase and propagation phase, which suffers from narrow bandwidth [37–39]. Here, we applied our concept of polarization-maintaining metasurfaces to encode complex phase profiles with geometric phase gradient metasurfaces and experimentally demonstrated arbitrary polarization holographic images with broadband characteristics.

RESULTS

Design method of polarization-maintaining metasurfaces

Our general concept of the proposed broadband polarization-addressing metasurfaces is illustrated in Fig. 1 (C and D) and compared with respect to the dispersive design in Fig. 1 (A and B). A 1-μm-thin GaN film on the x-y plane is etched to form rectangular pillars suitably disposed and oriented to acquire the desired geometric phase and shape a given incident CP into a deflected beam with opposite helicity. The excitation input light beam propagating along the $-z$ direction is chosen to be linearly polarized in the x direction and can thus be decomposed into two CP beams with equal amplitude and phase.

Université Cote d'Azur, CNRS, CRHEA, Rue Bernard Gregory, Sophia Antipolis, 06560 Valbonne, France.
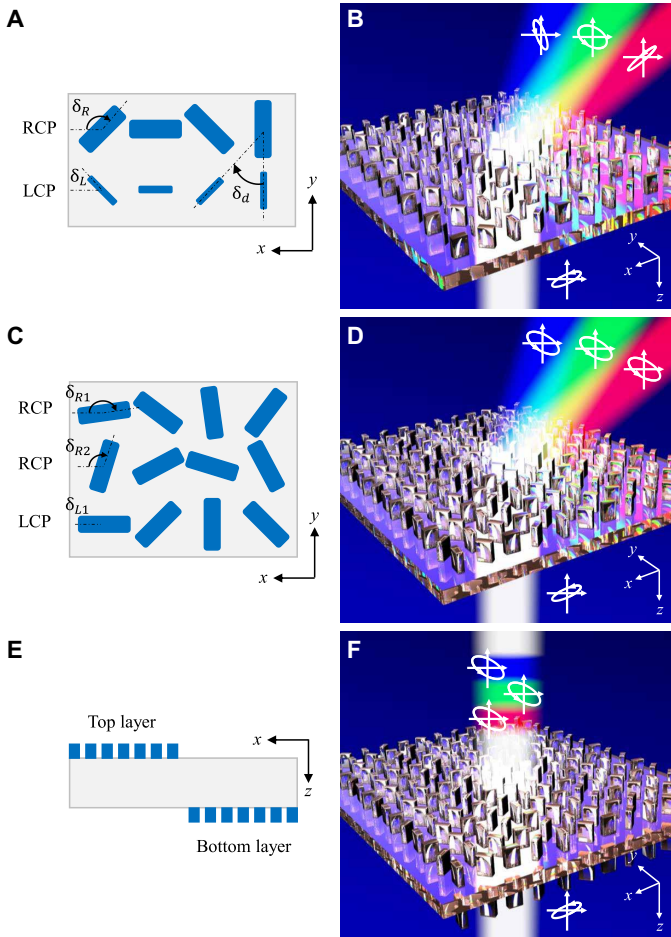*Corresponding author. Email: patrice.genevet@crhea.cnrs.fr

Fig. 1. Linear superposition of CP beams using phase gradient metasurfaces. (**A**) A linear superposition of right CP (RCP) and left CP (LCP) with different sizes of metastructures. (**B**) Schematic representation of the dispersive polarization response of the traditional polarization-controlling metasurfaces. (**C**) Broadband polarization-maintaining design consisting in combination of RCP, LCP, and LCP (or RCP, RCP, and LCP) realized with a uniform size metastructure. (**D**) Schematic representation of the broadband polarization-maintaining metasurfaces. (**E**) Angular nondispersive design with metasurface doublet. (**F**) Schematic representation of the angular nondispersive metasurfaces.

Note that the incident light can be arbitrary polarization except for two pure CP beams (see more details in notes S3 and S4). As considered in the literature (*22*), a single Pancharatnam−Berry (PB) phase gradient array is able to direct the two incident CP beams into deflected beams with opposite helicity accordingly to their incident polarization spin. In this first example (Fig. 1A), the dispersive case, the first metastructure line in the bottom of the metasurface is arranged counterclockwise with an orientation angle increment of δ_d to deflect the incident RCP into an LCP beam propagating at an angle of $\theta_{td} = \arcsin(\lambda\delta_d/\pi P)$, where λ is the operating wavelength and P is the period of the metastructures. The complex transmission of LCP beam is $a_1(\lambda)e^{i\varphi_1(\lambda)}e^{-i2\delta_L}$ (see eq. S3) with starting rotation angle (SOA) of δ_L, where the conversion efficiency $a_1(\lambda)$ and propagation phase $\varphi_1(\lambda)$ are usually dispersive and related to the size of the bottom metastructures, while the geometric phase $-2\delta_L$ is only related to the rotation angle of the metastructures. The additional metastructures disposed in the top line of the metasurface are arranged clockwise with the same

angle increment of δ_d to convert the LCP into an RCP beam propagating at the same angle of θ_{td}. The transmitted RCP has the complex amplitude of $a_2(\lambda)e^{i\varphi_2(\lambda)}e^{i2\delta_R}$ according to eq. S3 with SOA of δ_R, where $a_2(\lambda)$ and $\varphi_2(\lambda)$ are related to the size of the top metastructures. Therefore, the output state of polarization (SoP) can be described as

$$|n_{LR}\rangle = a_1(\lambda)e^{i\varphi_1(\lambda)}e^{-i2\delta_L}|+\rangle + a_2(\lambda)e^{i\varphi_2(\lambda)}e^{i2\delta_R}|-\rangle \quad (1)$$

The ellipticity angle becomes $\chi = \frac{1}{2}\arcsin\frac{a_2(\lambda)^2 - a_1(\lambda)^2}{a_2(\lambda)^2 + a_1(\lambda)^2}$, and the azimuth angle is $\psi = \frac{\varphi_2(\lambda) - \varphi_1(\lambda)}{2} + \delta_R + \delta_L$. Since $a_{1,2}(\lambda)$ and $\varphi_{1,2}(\lambda)$ are usually dispersive, the output polarization is related to the wavelength as shown in the schematic of Fig. 1B.

To address this problem, we propose an interesting superposition using three lines of phase gradient metasurface as shown in Fig. 1C. The broadband polarization-maintaining design consists of controlling the diffraction of one LCP and two RCP with SOA of δ_{L1}, δ_{R1}, and δ_{R2}. The key idea is to homogenize the dispersion effect using a unique metastructure, i.e., only one nanopillar with a uniform size, for all lines, so that all transmitted LCP and RCP beams share the same conversion efficiency $a(\lambda)$ and propagation phase $\varphi(\lambda)$. According to eq. S3, the output polarization can be written as

$$|n_{LRR}\rangle = a(\lambda)e^{i\varphi(\lambda)}e^{-i2\delta_{L1}}|+\rangle + a(\lambda)e^{i\varphi(\lambda)}e^{i2\delta_{R1}}|-\rangle +$$
$$a(\lambda)e^{i\varphi(\lambda)}e^{i2\delta_{R2}}|-\rangle = a(\lambda)e^{i\varphi(\lambda)}(e^{-i2\delta_{L1}}|+\rangle +$$
$$e^{i2\delta_{R1}}|-\rangle + e^{i2\delta_{R2}}|-\rangle) \quad (2)$$

It can be seen that the dispersive term $a(\lambda)e^{i\varphi(\lambda)}$ factorizes, leading to the generated polarization only related to the rotation angle of δ_{L1}, δ_{R1}, and δ_{R2}, yielding to a nondispersive polarization behavior with unlimited bandwidth as shown in the schematic of Fig. 1D. Note that the deflection efficiency, which depends on the polarization conversion efficiency of the building block, changes as a function of the incident wavelength. Further efforts in designing broadband half-waveplate nanostructure could be realized to improve the device performance over much larger spectral range. Since the diffracted angles of the converted light beam θ_{td} (eq. S7) of both the dispersive and nondispersive polarization design are angular dispersive, a metasurface doublet is designed to eliminate the angular dispersion as shown in Fig. 1 (E and F) (see more details in note S5).

Simulated results and dispersion analysis

We performed the numerical simulation of realistic nanostructures using full-wave finite-difference time domain. The metastructure consists of GaN nanopillars on a sapphire substrate as shown in Fig. 2 (A and B). The period of the metastructure is chosen to avoid spurious diffraction effects in the substrate as $P = 300$ nm, and the thickness of the GaN nanopillar is $h = 1$ μm (see more simulated results in fig. S5). To better explain the difference between our proposed broadband polarization-addressing method using a unique nanostructure size and the conventional dual-nanostructure reconstruction method, i.e., dispersive superposition obtained with different nanostructure sizes (*20*), we carried out numerical simulation for both methods as shown in Fig. 2. We first numerically calculated the polarization conversion efficiency $a(\lambda)$ (red and black lines) and propagation phase $\varphi(\lambda)$ (blue and green lines) with two different sizes of
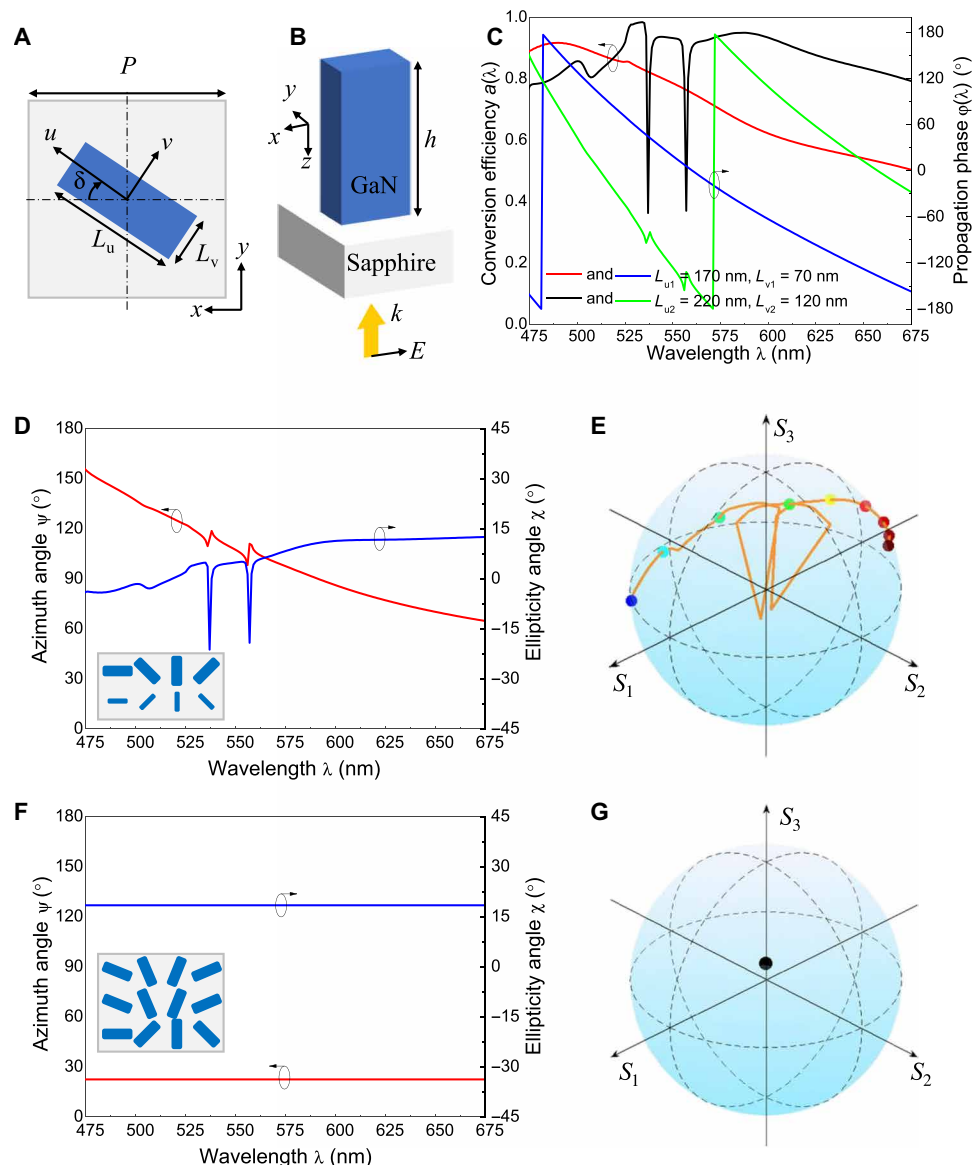
Fig. 2. Numerical simulation of the metasurfaces. (**A**) Top view and (**B**) perspective view of one metastructure. $P = 300$ nm and $h = 1000$ nm. (**C**) Simulated results of the polarization conversion efficiency $a(\lambda)$ (red and black lines) and propagation phase $\varphi(\lambda)$ (blue and green lines) with two different sizes of GaN nanopillars. Red and blue curves: $L_{u1} = 170$ nm and $L_{v1} = 70$ nm. Black and green curves: $L_{u2} = 220$ nm and $L_{v2} = 120$ nm. (**D**) Calculated azimuth angle and ellipticity angle of the output polarization and (**E**) the corresponding SoP on Poincaré sphere as a function of incident wavelength from 475 to 675 nm with dispersive superposition consisting of two different sizes of GaN nanopillars with zero SOA, indicating that the traditional linear superposition of opposite polarization leads to dispersive polarization response. (**F**) Calculated azimuth and ellipticity angles of the output polarization and (**G**) the corresponding SoP on Poincaré sphere as a function of incident wavelength from 475 to 675 nm with the proposed nondispersive superposition consisting of a uniform size of GaN nanopillars with $L_{u2} = 220$ nm, $L_{v2} = 120$ nm, $\delta_{L1} = 0°$, $\delta_{R1} = 22.5°$, and $\delta_{R2} = 22.5°$, indicating that an assembly of a generic building block could realize broadband polarization-maintaining behavior with unlimited bandwidth.

GaN nanopillars as shown in Fig. 2C. As expected, one can see that both $a(\lambda)$ and $\varphi(\lambda)$ are highly dependent on the size of the nanostructures. Thereafter, we simulated the azimuth angle and ellipticity angle of the output polarization as a function of the incident wavelength for both cases (Fig. 2, D and F, for dispersive case, calculated from Eq. 1, and polarization-maintaining case, calculated from Eq. 2, respectively) and the corresponding SoP on Poincaré sphere (Fig. 2, E and G, for dispersive case and polarization-maintaining case, respectively). The dispersive superposition relying on two

nanostructures with different sizes ($L_{u1} = 170$ nm, $L_{v1} = 70$ nm, and $\delta_L = 0°$ for the bottom line and $L_{u2} = 220$ nm, $L_{v2} = 120$ nm, and $\delta_R = 0°$ for the top line) exhibits strong wavelength-dependent SoP (Fig. 2E), since $a_{1,2}(\lambda)$ and $\varphi_{1,2}(\lambda)$ have different dispersive responses according to Fig. 2C. However, our design with a uniform size of GaN nanopillars ($L_{u2} = 220$ nm and $L_{v2} = 120$ nm) oriented at different starting angles to address the chosen SoP eliminates dispersion even in the presence of strong nanostructure dispersive response as shown in Fig. 2 (F and G) with $\delta_{L1} = 0°$, $\delta_{R1} = 22.5°$, and $\delta_{R2} = 22.5°$.

Full-polarization generation

Our superposition design not only addresses nondispersive polarization properties, but it can also generate arbitrary and full polarization with a uniform size of the metastructures. To simplify the discussion, we propose to refer it as LRR configuration (the design using one LCP and two RCP) as shown in Fig. 3A, consisting of phase gradient supercells with controllable SOA of δ_{L1}, δ_{R1}, and δ_{R2}. Since the output polarization is related to the relative phase difference between these three components, we fix δ_{L1} as zero. According to Eq. 2, the dispersive term $a(\lambda)e^{i}\varphi^{(\lambda)}$ factorizes, so the output SoP becomes $|n_{LRR}\rangle = |+\rangle + (e^{i2\delta_{R1}} + e^{i2\delta_{R2}})|-\rangle = |+\rangle + a_-e^{i\delta_-}|-\rangle$, where a_- and δ_- are the amplitude and phase of $(e^{i2\delta_{R1}} + e^{i2\delta_{R2}})$, respec-

tively. Therefore, the ellipticity angle becomes $\chi = \frac{1}{2}\arcsin\frac{a_-^2 - 1}{a_-^2 + 1}$, and the azimuth angle is $\psi = \frac{\delta_-}{2}$. The ellipticity and azimuth angles as a function of δ_{R2} are shown in Fig. 3 (B and C), respectively. Since $0 \leq a_- \leq 2$, the ellipticity angle of the SoP has an upper limit of $\frac{1}{2}\arcsin\frac{3}{5}$ (i.e., $-\frac{\pi}{4} \leq \chi \leq \frac{1}{2}\arcsin\frac{3}{5}$). The corresponding Poincaré sphere with $\delta_{R1} = 0°$, 30°, and 60° are shown in Fig. 3 (D to F), respectively. A full azimuth angle is realized as shown in Fig. 3G by controlling both δ_{R1} and δ_{R2} from 0° to 180°. Therefore, the generated SoPs cover the bottom sphere cap with $-\frac{\pi}{4} \leq \chi \leq \frac{1}{2}\arcsin\frac{3}{5}$. Likewise, the RLL configuration (one RCP and two LCP) shown in Fig. 3 (H to N) can generate SoPs that cover the top sphere cap with $-\frac{1}{2}\arcsin\frac{3}{5} \leq \chi \leq \frac{\pi}{4}$ as shown in Fig. 3N. In this way, depending on the choice of the
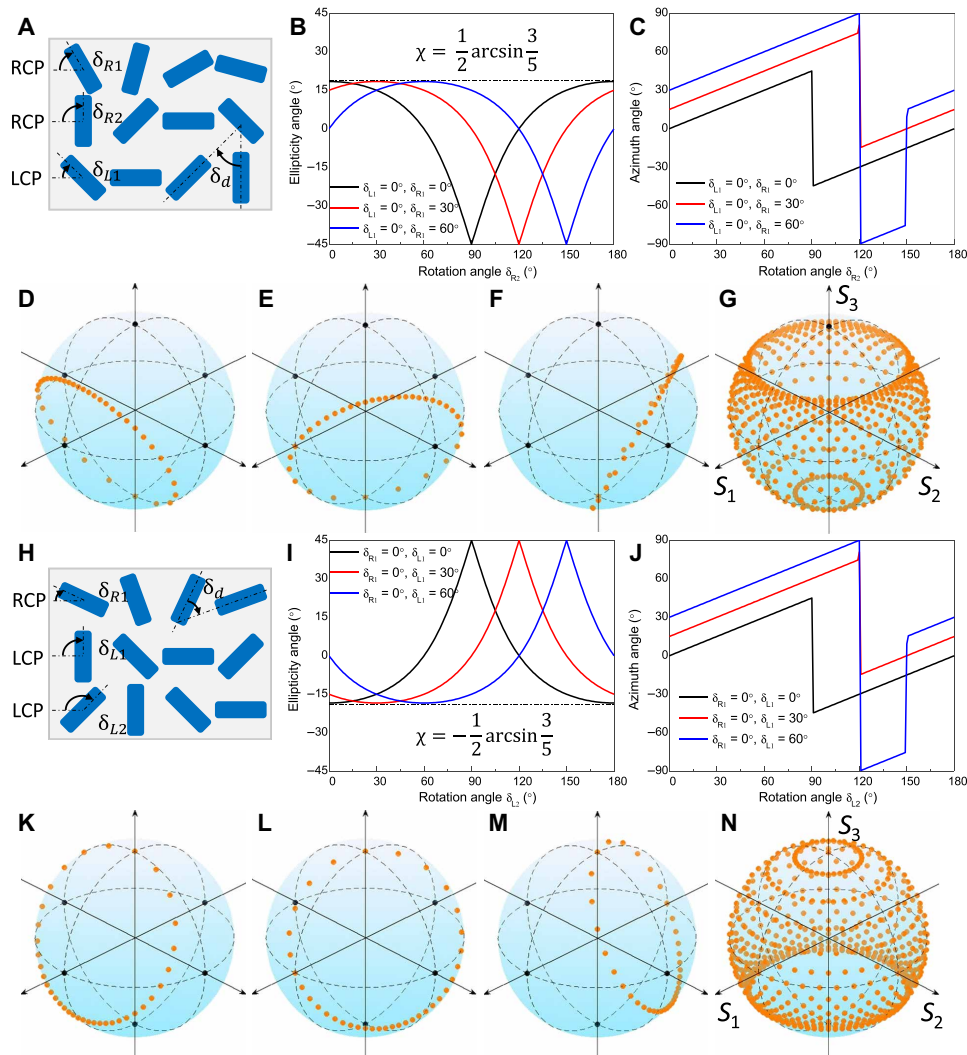

Fig. 3. Design of full-polarization pixels using geometric phase metasurface. (**A**) One supercell of the metasurface consists of one LCP and two RCP beams. (**B**) Ellipticity angle and (**C**) azimuth angle of the output light as a function of rotation angle δ_{R2} for fixed $\delta_{L1} = 0°$. Black curve: $\delta_{R1} = 0°$; red curve: $\delta_{R1} = 30°$; blue curve: $\delta_{R1} = 60°$. The corresponding Poincaré sphere when (**D**) $\delta_{R1} = 0°$, (**E**) $\delta_{R1} = 30°$, and (**F**) $\delta_{R1} = 60°$. (**G**) By controlling both δ_{R1} and δ_{R2} from 0° to 180°, the SoP covers the bottom sphere cap of Poincaré sphere with $-\frac{\pi}{4} \leq \chi \leq \frac{1}{2}\arcsin\frac{3}{5}$. (**H**) One supercell of metasurface consists of one RCP and two LCP beams. (**I**) Ellipticity angle and (**J**) orientation angle of the output light as a function of rotation angle δ_{L2} for fixed $\delta_{R1} = 0°$. Black curve: $\delta_{R1} = 0°$; red curve: $\delta_{R1} = 30°$; blue curve: $\delta_{R1} = 60°$. The corresponding Poincaré sphere when (**K**) $\delta_{R1} = 0°$, (**L**) $\delta_{R1} = 30°$, and (**M**) $\delta_{R1} = 60°$. (**N**) By controlling both δ_{L1} and δ_{L2} from 0° to 180°, the SoP covers the top sphere cap of Poincaré sphere with $-\frac{1}{2}\arcsin\frac{3}{5} \leq \chi \leq \frac{\pi}{4}$. (G) and (N) indicate that the superposition of CPs diffracted by array of a generic PB building block could produce any arbitrary SoP, without having to carefully engineers the metastructure geometry for the desired application.

desired diffracted state of polarization, one could choose in the LRR and RLL configurations, leading to full-polarized and broadband properties of output light. Note that using twofold superposition with a uniform metastructure, the dispersion term in Eq. 1 can also be factorized, i.e., $a_1(\lambda)e^{i\varphi_1(\lambda)} = a_2(\lambda)e^{i\varphi_2(\lambda)}$, leading to a nondispersive property but only for linear output polarization.

Unlimited bandwidth polarization-maintaining meta-hologram

As a proof of principle, we design four elliptical polarizations using the above mentioned LRR and RLL configurations as shown in Fig. 4. The deflector is pixelated into pixel array containing four metastructures in x direction and three lines in y direction, per pixel. By encoding the holographic phase profiles into pixelated metasurfaces, we are able to generate holographic images with arbitrary polarization and broadband characteristics. The details of the rotation angles and the corresponding ellipticities and azimuth angles are shown in the table S1. We encode the holographic phase profiles to exhibit four playing card suits of "spade," "heart," "club," and "diamond." Scanning electron microscopy (SEM) images of the fabricated metasurfaces with top and tilt view is shown in Fig. 4 (A and B). The measured holographic images illuminated with coherent laser source at $\lambda = 600$ nm are shown in Fig. 4C (see more details of fabrication processes and measurement setup in Materials and Methods and figs. S9 and S11). The measured SoP is plotted as blue dots in the Poincaré sphere as shown in Fig. 4D, which agrees well with the

designed SoP denoted by the red dots. The broadband response of the polarization is demonstrated in Fig. 5. The holographic images of spade with the incident wavelength ranging from $\lambda = 475$ nm to 675 nm are shown in the left panels of Fig. 5 (A to I). To characterize the polarization on a broadband wavelength range, we have selected a Thorlabs mounted Superachromatic quarter waveplate (AQWP05M-600) with rotation angle of $\theta_{\lambda/4} = 67.5°$ and a broadband Thorlabs linear polarizer (WP25M-VIS) with rotation angle of $\theta_{LP} = 49.07°$ that were positioned between the meta-hologram and the projector to block the holographic images of designed SoP (details of setup are shown in the fig. S11). With this choice of waveplate/polarizer orientations, holographic images are almost totally blocked in the entire visible range as shown in the right panels of Fig. 5 (A to I), thus confirming the exceptional broadband response of our polarization-maintaining design approach. The viewing angle of the holographic image is related to the operating wavelength as $\Theta = 2 \arcsin(\lambda/2P_h)$, where P_h is the pixel size of the hologram. Therefore, the blue holographic image has smaller size than the red holographic image. To further quantify experimentally the SoP, we projected the holographic images into a broadband polarimeter, which indicated that the SoP is correctly maintained around the designed value as shown in Fig. 5J. Since the pixel size of the meta-hologram is larger than the operating wavelength, there are higher-order images generated, which decrease the efficiency of the interested order as measured in Fig. 5K. It is possible to increase the efficiency by decreasing the pixel size to subwavelength scale. We have added a simulation proving that
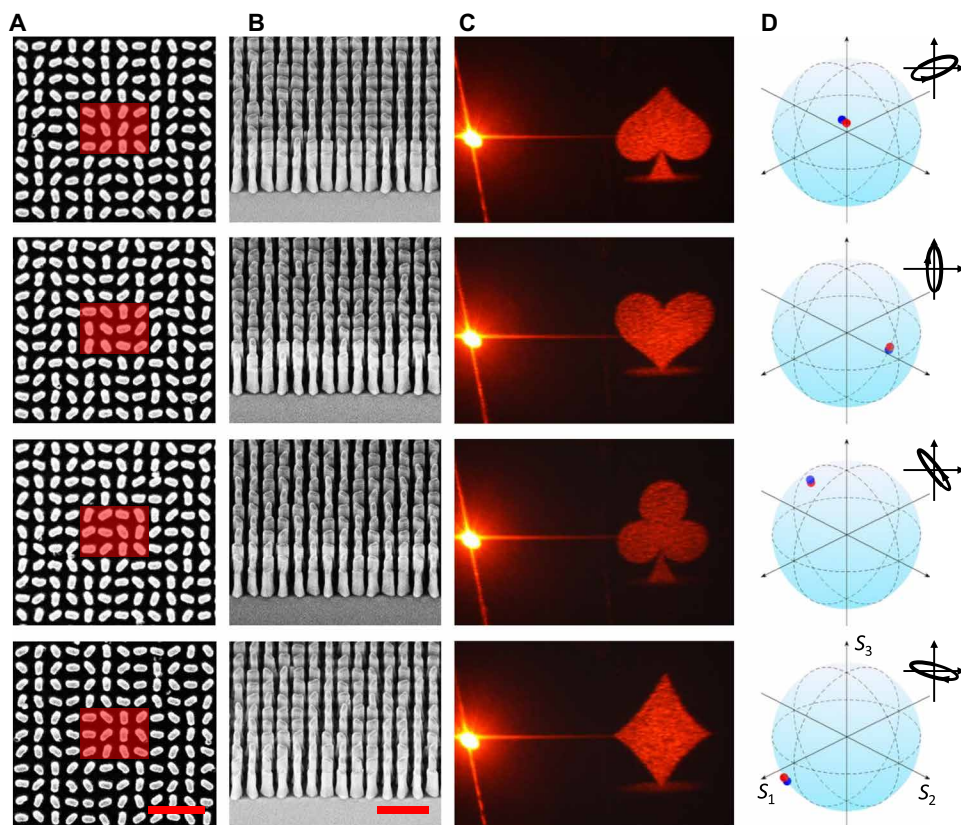

Fig. 4. Full polarized meta-hologram. (**A**) Top view and (**B**) tilt view of the SEM images of the metasurfaces. The red rectangular highlight area in (A) shows one pixel of the meta-holograms. (**C**) Measured holographic images (illumination at $\lambda = 600$ nm) of the meta-holograms. (**D**) Measured SoP on Poincaré sphere. Red dots, designed value; blue dots, measured value. Scale bars, 1 μm (A and B).
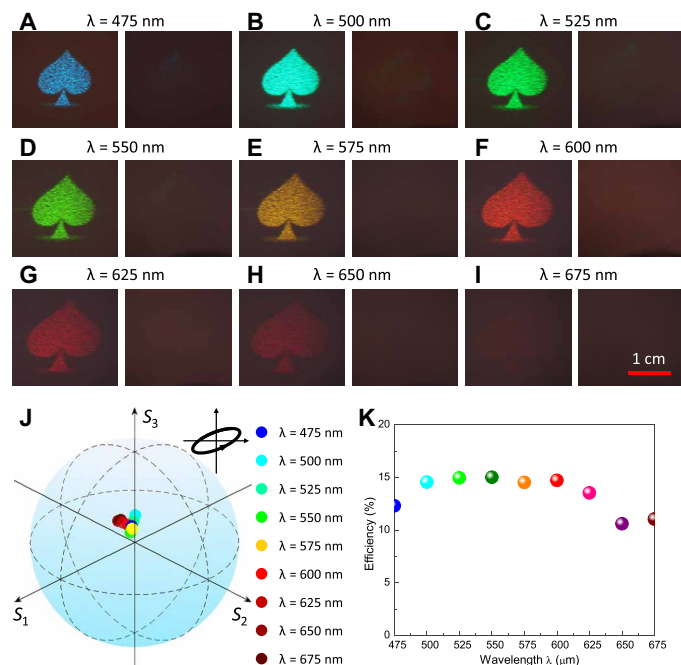
Fig. 5. Broadband polarization-maintaining properties of the nondispersive metasurface. (**A** to **I**) Measured holographic images with the incident wavelength from 475 to 675 nm (left: without analyzer; right: with broadband quarter wave-plate at $\theta_{\lambda/4} = 67.5°$ and linear polarizer (LP) at $\theta_{LP} = 49.07°$ to block the holographic images). The holographic images in the right panels are almost totally blocked in the entire visible range, confirming the exceptional broadband response of out polarization–maintaining design approach. (**J**) Measured SoP at different wavelengths agrees well to the designed value in Fig. 2G. (**K**) Measured efficiency is higher than 10% across the entire visible range.

higher efficiency with subwavelength pixel size is achievable, referring to fig. S6. Note that the unlimited bandwidth of polarization-maintaining behavior is conserved for all of the input polarization (see details in note S2). The only limitation of our design approach concerns the addressing of arbitrary polarization state that are realized for all of the input polarization except for two pure input CP beams (see details in note S4).

Angular nondispersive wavefront shaping using cascaded metasurface

According to eq. S7, the deflection angle is, in general, subjected to the incident wavelength, i.e., in other words, the deflection function of the device remains chromatically dispersive. However, this angle-dependent dispersive response can be treated using appropriate combination of metasurfaces with refractive dispersive materials (*40*), which would resolve this issue (see more details in note S5). The idea to address chromatic angular dispersion is straightforward and consists in using cascaded parallel metasurfaces, designed for $\alpha = 0°$ (see definition of α in fig. S7A), as shown in Fig. 6A. Thus, the transmitted angle can be described from eq. S27 as

$$\theta_t = \arcsin\left(\frac{\lambda\delta_d}{\pi P} + \frac{\lambda\delta_d'}{\pi P}\right) \qquad (3)$$

It can be seen that when the increment rotation angle of the two metasurfaces are opposite ($\delta_d = -\delta_d'$), i.e., when the angular dispersive properties of each metasurfaces compensate, a constant
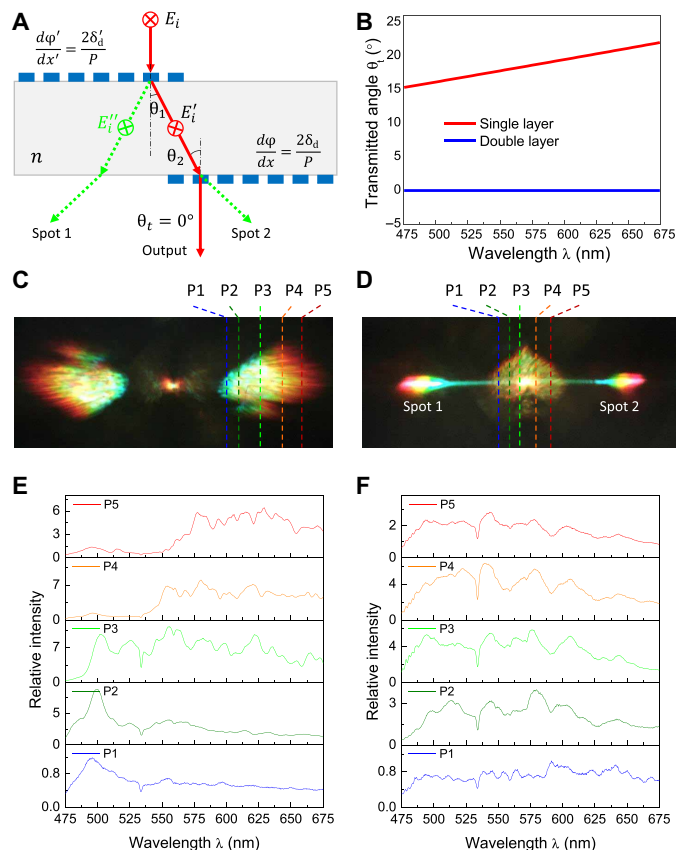

Fig. 6. Angular nondispersive wavefront shaping using cascaded metasurface doublet. (**A**) Schematic of angular nondispersive design using two layers of metasurfaces on both sides of a sapphire substrate. The phase gradient of the two-layer metasurfaces are $\frac{d\varphi'}{dx'} = \frac{2\delta_d'}{P}$ on the top and $\frac{d\varphi}{dx} = \frac{2\delta_d}{P}$ on the bottom with $\delta_d = -\delta_d' = 30°$. A linearly broadband light is normally illuminated from the top metasurface and diffracted to the bottom metasurface. Two spots are generated from the top deflector as shown in the green optical path. (**B**) Transmitted angle with single-layer metasurface (red curve) and double-layer metasurfaces (blue curve). A nondispersive angle response is realized in unlimited bandwidth using double-layer metasurfaces. Measurement results of the holographic image of spade using (**C**) single-layer metasurface and (**D**) double-layer metasurfaces. The holograms are imaged at the entrance slit of a spectrometer for spectrum characterization. A slit with 20 μm in width is placed to select a line of the image light at specific position of P1, P2, … P5. The corresponding spectra for (**E**) dispersive case and (**F**) nondispersive case at position P1 to P5 show a red shift of the bandwidth for large angle in (E), while (F) spectra are essentially broadband.

transmission angle $\theta_t = 0°$ is obtained, leading to a perfect angular nondispersive metasurface with unlimited bandwidth and without any additional approximations as shown in Fig. 6B. The fabrication details and results are shown in fig. S10. The same optical setup of fig. S11 is used here to capture the angular nondispersive holographic image, but the transmitted angle of the image is zero. The experimental results of the dispersive and nondispersive holographic images are shown in Fig. 6 (C and D), respectively. Two spots observed at the exit of the doublet, as shown in Fig. 6D, are induced by the first layer of deflector as shown in the green light path in Fig. 6A (explaining the weaker intensity on right spot with respect to left counterpart). The holographic images are then projected at the entrance slit of a spectrometer to perform spectrum characterization

at specific position along the image located at P1, P2, … P5 (which is chosen from left edge to the right edge of the image) as shown in Fig. 6 (C and D). As it is expected for the dispersive case, the spectrum of the hologram red shift according to the angular dispersion law for larger deflection angles, as shown in Fig. 6E. Therefore, P1 has more intensity in the blue range, while P5 has more in the red range. Note that the relative intensities in P1 to P5 are changing because of the size of the actual portion of the image considered in the experiment. Comparatively, the nondispersive and polarization-maintaining case, all spectra always remain broadband at all the positions across the image as shown in Fig. 6F.

DISCUSSION

In conclusion, we have demonstrated a general method of full-polarization generation and bandwidth-unlimited polarization-maintaining diffractive planar optics. It relies on the superposition of orthogonal polarizations generated by PB phase metasurfaces composed of a unique element to eliminate the dispersive response of the structures. By linear superposition of amplitude-controlled polarization handiness, using RLL and LRR configurations, full-polarization generation is established over an exceptionally unlimited bandwidth, experimentally demonstrated across the entire visible range from 475 to 675 nm. The realization of a metasurface doublet, involving an additional beam deflector with opposite deflection properties, is shown to address both the angular and the polarization chromatic dispersion over an extremely large bandwidth. The capability of generating and maintaining any arbitrary state of polarization on the entire visible range would lead to a plethora of promising applications in full-color displays, augmented/virtual reality display, broadband polarization camera, vector beam generation, visible light communication, etc.

MATERIALS AND METHODS
Device fabrication

The fabrication processes are shown in fig. S9. A molecular beam epitaxy (MBE) Riber system is used to grow GaN thin film with 1 μm in thickness on a double-side polished c-plan sapphire substrate. The GaN nanopillars are patterned using conventional electron beam lithography processes. We spin-coat ~180 nm of polymethyl methacrylate (PMMA) resist (495A4) on the GaN thin film and bake it on a hot plate at a temperature of 125°C. The PMMA resist is exposed with designed patterns using electron beam lithography at 20 keV (Raith Elphy Plus, Zeiss Supra 40) and developed using 3:1 isopropyl alcohol:methyl isobutyl ketone solution. Subsequently, a 50-nm-thick Ni is deposited on the sample using E-beam evaporation. After lift-off process by immersing the sample into acetone solution for 2 hours, a Ni hard mask is obtained. The GaN nanorods are created by reactive ion etching (Oxford System) with a plasma composed of Cl_2CH_4Ar gases, followed by chemical etching with 1:1 $H_2O_2:H_2SO_4$ solution to remove the Ni hard mask, revealing a GaN nanopillar array.

Optical setup

The optical setup for meta-hologram characterization is shown in fig. S11. A laser beam propagates through a broadband linear polarizer (WP25M-VIS) with axis of transmission in horizontal direction to generate linear polarized input beam. It is weakly focused by an achromatic lens with a focal length of 50 mm onto the meta-hologram,

which is mounted on a three-dimensional translation stage. The holographic image is projected onto a projector placed 10 cm away from the meta-hologram. A broadband quarter waveplate with fast axis at angle $\theta_{\lambda/4}$ and a broadband linear polarizer with axis of transmission at angle θ_{LP} are used to block selected images. We assume an incident beam $\vec{E}_{in}$ propagates through the selected quarter waveplate and linear polarizer and describe the output electric field $\vec{E}_{out}$ as $\vec{E}_{out} = A_{LP}(\theta_{LP}) A_{\lambda/4}(\theta_{\lambda/4}) \vec{E}_{in}$. Selected rotation angles $\theta_{\lambda/4}$ and θ_{LP} are chosen to block the specific output images (i.e., $\vec{E}_{out} = 0$).

SUPPLEMENTARY MATERIALS

Supplementary material for this article is available at http://advances.sciencemag.org/cgi/content/full/7/5/eabe1112/DC1

REFERENCES AND NOTES

1. N. Yu, P. Genevet, M. A. Kats, F. Aieta, J.-P. Tetienne, F. Capasso, Z. Gaburro, Light propagation with phase discontinuities: Generalized laws of reflection and refraction. *Science* **334**, 333–337 (2011).
2. P. Genevet, F. Capasso, F. Aieta, M. Khorasaninejad, R. Devlin, Recent advances in planar optics: From plasmonic to dielectric metasurfaces. *Optica* **4**, 139–152 (2017).
3. G. Li, S. Zhang, T. Zentgraf, Nonlinear photonic metasurfaces. *Nat. Rev. Mater.* **2**, 17010 (2017).
4. Q. H. Song, W. M. Zhu, P. C. Wu, W. Zhang, Q. Y. S. Wu, J. H. Teng, Z. X. Shen, P. H. J. Chong, Q. X. Liang, Z. C. Yang, D. P. Tsai, T. Bourouina, Y. Leprince-Wang, A. Q. Liu, Liquid-metal-based metasurface for terahertz absorption material: Frequency-agile and wide-angle. *APL Mater.* **5**, 066103 (2017).
5. P. Genevet, D. Wintz, A. Ambrosio, A. She, R. Blanchard, F. Capasso, Controlled steering of Cherenkov surface plasmon wakes with a one-dimensional metamaterial. *Nat. Nanotechnol.* **10**, 804–809 (2015).
6. L. Yan, W. Zhu, M. F. Karim, H. Cai, A. Y. Gu, Z. Shen, P. H. J. Chong, D.-L. Kwong, C.-W. Qiu, A. Q. Liu, 0.2 λ₀ Thick adaptive retroreflector made of spin-locked metasurface. *Adv. Mater.* **30**, 1802721 (2018).
7. Q. H. Song, P. C. Wu, W. M. Zhu, W. Zhang, Z. X. Shen, P. H. J. Chong, Q. X. Liang, D. P. Tsai, T. Bourouina, Y. Leprince-Wang, A. Q. Liu, Split Archimedean spiral metasurface for controllable GHz asymmetric transmission. *Appl. Phys. Lett.* **114**, 151105 (2019).
8. J. Jang, H. Jeong, G. Hu, C.-W. Qiu, K. T. Nam, J. Rho, Kerker-conditioned dynamic cryptographic nanoprints. *Adv. Opt. Mater.* **7**, 1801070 (2019).
9. M. A. Ansari, I. Kim, D. Lee, M. H. Waseem, M. Zubair, N. Mahmood, T. Badloe, S. Yerci, T. Tauqeer, M. Q. Mehmood, J. Rho, A spin-encoded all-dielectric metahologram for visible light. *Laser Photonics Rev.* **13**, 1900065 (2019).
10. M. A. Ansari, I. Kim, I. D. Rukhlenko, M. Zubair, S. Yerci, T. Tauqeer, M. Q. Mehmood, J. Rho, Engineering spin and antiferromagnetic resonances to realize an efficient direction-multiplexed visible meta-hologram. *Nanoscale Horiz.* **5**, 57–64 (2019).
11. S. Wang, P. C. Wu, V.-C. Su, Y.-C. Lai, M.-K. Chen, H. Y. Kuo, B. H. Chen, Y. H. Chen, T.-T. Huang, J.-H. Wang, R.-M. Lin, C.-H. Kuan, T. Li, Z. Wang, S. Zhu, D. P. Tsai, A broadband achromatic metalens in the visible. *Nat. Nanotechnol.* **13**, 227–232 (2018).
12. J. Y. H. Teo, L. J. Wong, C. Molardi, P. Genevet, Controlling electromagnetic fields at boundaries of arbitrary geometries. *Phys. Rev. A* **94**, 023820 (2016).
13. A. Tittl, A. Leitis, M. Liu, F. Yesilkoy, D.-Y. Choi, D. N. Neshev, Y. S. Kivshar, H. Altug, Imaging-based molecular barcoding with pixelated dielectric metasurfaces. *Science* **360**, 1105–1109 (2018).
14. Y. Z. Shi, S. Xiong, Y. Zhang, L. K. Chin, Y.-Y. Chen, J. B. Zhang, T. H. Zhang, W. Ser, A. Larrson, S. H. Lim, J. H. Wu, T. N. Chen, Z. C. Yang, Y. L. Hao, B. Liebberg, P. H. Yap, K. Wang, D. P. Tsai, C.-W. Qiu, A. Q. Liu, Sculpting nanoparticle dynamics for single-bacteria-level screening and direct binding-efficiency measurement. *Nat. Commun.* **9**, 815 (2018).
15. Q. Song, S. Khadir, S. Vézian, B. Damilano, P. de Mierry, S. Chenot, V. Brandli, R. Laberdesque, B. Wattellier, P. Genevet, Printing polarization and phase at the optical diffraction limit: Near- and far-field optical encryption. *Nanophotonics* **10**, 697–704 (2020).
16. C. Pfeiffer, C. Zhang, V. Ray, L. J. Guo, A. Grbic, High performance bianisotropic metasurfaces: Asymmetric transmission of light. *Phys. Rev. Lett.* **113**, 023902 (2014).
17. Y. Zhao, M. A. Belkin, A. Alù, Twisted optical metamaterials for planarized ultrathin broadband circular polarizers. *Nat. Commun.* **3**, 870 (2012).
18. N. Yu, F. Aieta, P. Genevet, M. A. Kats, Z. Gaburro, F. Capasso, A broadband background-free quarter-wave plate based on plasmonic metasurfaces. *Nano Lett.* **12**, 6328–6333 (2012).
19. P. C. Wu, W.-Y. Tsai, W. T. Chen, Y.-W. Huang, T.-Y. Chen, J.-W. Chen, C. Y. Liao, C. H. Chu, G. Sun, D. P. Tsai, Versatile polarization generation with an aluminum plasmonic metasurface. *Nano Lett.* **17**, 445–452 (2017).

20. Q. Song, A. Baroni, R. Sawant, P. Ni, V. Brandli, S. Chenot, S. Vézian, B. Damilano, P. de Mierry, S. Khadir, P. Ferrand, P. Genevet, Ptychography retrieval of fully polarized holograms from geometric-phase metasurfaces. *Nat. Commun.* **11**, 2651 (2020).

21. P. Genevet, F. Capasso, Holographic optical metasurfaces: A review of current progress. *Rep. Prog. Phys.* **78**, 024401 (2015).

22. G. Zheng, H. Mühlenbernd, M. Kenney, G. Li, T. Zentgraf, S. Zhang, Metasurface holograms reaching 80% efficiency. *Nat. Nanotechnol.* **10**, 308–312 (2015).

23. Z.-L. Deng, J. Deng, X. Zhuang, S. Wang, T. Shi, G. P. Wang, Y. Wang, J. Xu, Y. Cao, X. Wang, X. Cheng, G. Li, X. Li, Facile metagrating holograms with broadband and extreme angle tolerance. *Light Sci. Appl.* **7**, 78 (2018).

24. L. Huang, S. Zhang, T. Zentgraf, Metasurface holography: From fundamentals to applications. *Nanophotonics* **7**, 1169–1190 (2018).

25. Y. Yuan, K. Zhang, B. Ratni, Q. Song, X. Ding, Q. Wu, S. N. Burokur, P. Genevet, Independent phase modulation for quadruplex polarization channels enabled by chirality-assisted geometric-phase metasurfaces. *Nat. Commun.* **11**, 4186 (2020).

26. Y.-W. Huang, W. T. Chen, W.-Y. Tsai, P. C. Wu, C.-M. Wang, G. Sun, D. P. Tsai, Aluminum plasmonic multicolor meta-hologram. *Nano Lett.* **15**, 3122–3127 (2015).

27. Z.-L. Deng, G. Li, Metasurface optical holography. *Mater. Today Phys.* **3**, 16–32 (2017).

28. Z. Li, I. Kim, L. Zhang, M. Q. Mehmood, M. S. Anwar, M. Saleem, D. Lee, K. T. Nam, S. Zhang, B. Luk'yanchuk, Y. Wang, G. Zheng, J. Rho, C.-W. Qiu, Dielectric meta-holograms enabled with dual magnetic resonances in visible light. *ACS Nano* **11**, 9382–9389 (2017).

29. R. Zhao, B. Sain, Q. Wei, C. Tang, X. Li, T. Weiss, L. Huang, Y. Wang, T. Zentgraf, Multichannel vectorial holographic display and encryption. *Light Sci. Appl.* **7**, 95 (2018).

30. F. Dong, H. Feng, L. Xu, B. Wang, Z. Song, X. Zhang, L. Yan, X. Li, Y. Tian, W. Wang, L. Sun, Y. Li, W. Chu, Information encoding with optical dielectric metasurface via independent multichannels. *ACS Photonics* **6**, 230–237 (2019).

31. X. Zang, F. Dong, F. Yue, C. Zhang, L. Xu, Z. Song, M. Chen, P.-Y. Chen, G. S. Buller, Y. Zhu, S. Zhuang, W. Chu, S. Zhang, X. Chen, Polarization encoded color image embedded in a dielectric metasurface. *Adv. Mater.* **30**, 1707499 (2018).

32. F. Yue, D. Wen, J. Xin, B. D. Gerardot, J. Li, X. Chen, Vector vortex beam generation with a single plasmonic metasurface. *ACS Photonics* **3**, 1558–1563 (2016).

33. A. Shaltout, J. Liu, V. M. Shalaev, A. V. Kildishev, Optically active metasurface with non-chiral plasmonic nanoantennas. *Nano Lett.* **14**, 4426–4431 (2014).

34. Q. Guo, C. Schlickriede, D. Wang, H. Liu, Y. Xiang, T. Zentgraf, S. Zhang, Manipulation of vector beam polarization with geometric metasurfaces. *Opt. Express* **25**, 14300–14307 (2017).

35. Z.-L. Deng, J. Deng, X. Zhuang, S. Wang, K. Li, Y. Wang, Y. Chi, X. Ye, J. Xu, G. P. Wang, R. Zhao, X. Wang, Y. Cao, X. Cheng, G. Li, X. Li, Diatomic metasurface for vectorial holography. *Nano Lett.* **18**, 2885–2892 (2018).

36. Z. Deng, M. Jin, X. Ye, S. Wang, T. Shi, J. Deng, N. Mao, Y. Cao, B.-O. Guan, A. Alù, G. Li, X. Li, Full-color complex-amplitude vectorial holograms based on multi-freedom metasurfaces. *Adv. Funct. Mater.* 1910610 (2020).

37. A. Arbabi, Y. Horie, M. Bagheri, A. Faraon, Dielectric metasurfaces for complete control of phase and polarization with subwavelength spatial resolution and high transmission. *Nat. Nanotechnol.* **10**, 937–943 (2015).

38. E. Arbabi, S. M. Kamali, A. Arbabi, A. Faraon, Vectorial holograms with a dielectric metasurface: Ultimate polarization pattern generation. *ACS Photonics* **6**, 2712–2718 (2019).

39. J. P. Balthasar Mueller, N. A. Rubin, R. C. Devlin, B. Groever, F. Capasso, Metasurface polarization optics: Independent phase control of arbitrary orthogonal states of polarization. *Phys. Rev. Lett.* **118**, 113901 (2017).

40. R. Sawant, P. Bhumkar, A. Y. Zhu, P. Ni, F. Capasso, P. Genevet, Mitigating chromatic dispersion with hybrid optical metasurfaces. *Adv. Mater.* **31**, 1805555 (2018).

Citation: Q. Song, S. Khadir, S. Vézian, B. Damilano, P. D. Mierry, S. Chenot, V. Brandli, P. Genevet, Bandwidth-unlimited polarization-maintaining metasurfaces. *Sci. Adv.* **7**, eabe1112 (2021).